



LAWRENCE
LIVERMORE
NATIONAL
LABORATORY

Stochastic Inversion of InSAR Data to Assess the Probability of Pressure Penetration into the Lower Caprock at In Salah

A. Ramirez, W. Foxall

May 28, 2014

International Journal of Greenhouse Gas Control

Disclaimer

This document was prepared as an account of work sponsored by an agency of the United States government. Neither the United States government nor Lawrence Livermore National Security, LLC, nor any of their employees makes any warranty, expressed or implied, or assumes any legal liability or responsibility for the accuracy, completeness, or usefulness of any information, apparatus, product, or process disclosed, or represents that its use would not infringe privately owned rights. Reference herein to any specific commercial product, process, or service by trade name, trademark, manufacturer, or otherwise does not necessarily constitute or imply its endorsement, recommendation, or favoring by the United States government or Lawrence Livermore National Security, LLC. The views and opinions of authors expressed herein do not necessarily state or reflect those of the United States government or Lawrence Livermore National Security, LLC, and shall not be used for advertising or product endorsement purposes.

Stochastic Inversion of InSAR Data to Assess the Probability of Pressure Penetration into the Lower Caprock at In Salah

Abelardo Ramirez¹ and William Foxall^{1,2}

1-Lawrence Livermore National Laboratory, Livermore, CA, USA, 94550,
2-Present address: Lawrence Berkeley National Laboratory, Berkeley, CA,
USA, 94720

Corresponding author:
Abelardo Ramirez
Lawrence Livermore National Laboratory
P.O. Box 808, L-046
Livermore, CA 94550
925-422-6909 (ph), 925-422-3925 (Fax)
ramirez3@llnl.gov

Abstract

We carried out stochastic inversions of InSAR data to assess the probability that pressure perturbations resulting from CO₂ injection into well KB-502 at In Salah penetrated into the lower caprock seal above the reservoir. We employed inversions of synthetic data to evaluate the factors that affect the vertical resolution of overpressure distributions, and to assess the impact of various sources of uncertainty in prior constraints on inverse solutions. These include alternative pressure-driven deformation modes within reservoir and caprock, the geometry of a sub-vertical fracture zone in the caprock identified in previous studies, and imperfect estimates of the rock mechanical properties. Inversions of field data indicate that there is a high probability that a pressure perturbation during the first phase of injection extended upwards along the fracture zone ~150 m above the reservoir, and less than 50% probability that it reached the Hot Shale unit at 1500 m depth. Within the uncertainty bounds considered, we conclude that it is very unlikely that the pressure perturbation approached within 150 m of the top of the lower caprock at the

Hercynian Unconformity. The results are consistent with previous deterministic inversion and forward modeling studies.

Keywords:

Markov Chain Monte Carlo, InSAR data, CO₂ sequestration, Leakage probability, Monitoring

1.0 INTRODUCTION

Inversion and modeling of the surface deformation caused by CO₂ injection at the In Salah field in Algeria imaged using Interferometric Synthetic Aperture Radar Interferometry (InSAR) have demonstrated the potential of InSAR as a powerful, cost effective tool for long-term monitoring of commercial-scale geological carbon sequestration in even relatively deep reservoirs. The InSAR images have been used as one of the primary data sets in several inversion and forward modeling studies to map the spatial distributions of subsurface changes in fluid volume and pressure and CO₂ saturation during the first period of active injection between 2004 and 2007 and the subsequent period of well shut-in. An important consensus of these studies is that the dominant flow within the reservoir in the vicinity of at least one of the In Salah wells is along a sub-vertical, narrow tabular zone that intersects the injection interval, and that changes in fluid pressure resulting from the injection penetrated up this zone into the lower caprock above the storage complex (the sandstone reservoir and the tight sandstone /siltstone unit overlaying it). However, because the vertical resolution of deformation models constrained by the surface displacement data is limited, the vertical extent of the pressure perturbation remains a subject of debate. The primary objective of the present paper is to evaluate the influence of factors specific to In Salah on the uniqueness of inverse solutions and forward models constrained by the InSAR data, and to provide probability estimates of the depth of overpressure penetration. These provide a

quantitative measure of uncertainty that could form the basis for risk-based decision making.

The In Salah project has been described in several papers (e.g. Wright et al., 2006; Ringrose et al., 2009; Vasco et al., 2010), and is briefly summarized here. In Salah is the world's first industrial-scale CO₂ storage project that from 2004 until 2011 injected 3.8 million tonnes of CO₂ captured from gas produced from the Krechba field. The injection took place through three wells (Figure 1) into a ~20 m thick Carboniferous sandstone formation (C10.2) on the flanks of an anticline at about 1800 m depth. The Krechba stratigraphic section is summarized in Figure 2. The storage complex at In Salah comprises this sandstone and the sandstone and siltstone unit (C10.3) overlying it. Above that a 900 m-thick sequence of Carboniferous mudstones and shales form a lower caprock seal.

Permanent-scatterer InSAR (PSInSAR; Ferretti et al, 2001) processing of Envisat data carried out by Tele-Rilevamento Europa (TRE) for the period from 2003 to early 2009 are described in Vasco et al. (2008, 2010) and Rucci et al. (2013). This period includes the first phase of injection into well KB-502 (Figure 1), and the subsequent well shut-in. Ferretti et al. (2011) describe the SqueeSARTM processing technique used to produce interferograms covering the second phase of injection at KB-502 beginning in November 2009. InSAR processing employing different techniques was also carried out by MacDonald, Detwiler and Associates in partnership with Haliburton-Pinnacle (Davis, 2011) and by Onuma and Ohkawa (2009) and Onuma et al. (2011). General explanations of the basic theory and implementation of InSAR are given in, for example, Burgmann et al. (2000) and Rosen et al. (2000)

In the first study to utilize the InSAR data, Vasco et al. (2008) inverted a time series of scalar line-of-sight range change (LOS) measurements between July 2003 and March 2007 to map fluid volume and pressure changes resulting from injection into KB-502. Fluid flow and pressurization were assumed to be restricted to the primary C10.2 reservoir. However, in a later study Vasco et al. (2010) interpreted the distinctive

double-lobe pattern of InSAR range change produced by injection into KB-502 as suggestive of pressure-driven tensile (Mode I) opening of a NW-striking fault or fracture zone within and/or above and below the reservoir horizon (see also Morris et al., 2011), and inverted the data for Mode I opening within this zone as well as isotropic volume changes within the reservoir. The inferred presence of such a zone of high permeability is consistent with the conclusions of Ringrose et al., (2009) and Iding and Ringrose (2010) that the dominant flow within the reservoir in the vicinity of KB-502 was along a near-vertical zone oriented NW, in the direction of maximum horizontal stress. This interpretation was subsequently supported by the identification of a NW-trending lineament on 3D seismic surfaces at the top of the C10.2 and on shallower horizons up to the Hot Shale (Figure 2) (Gibson-Poole and Raikes, 2010). The ~4 km long, ~300-400 m wide lineament intersects the trace of the horizontal section of KB-502 and coincides with the trough between the lobes in the InSAR pattern. A similar feature is seen extending SE from KB-503 on the C20.1 and C20.4 surfaces. The origin of the lineaments has not been determined conclusively, and their definition at shallower depths is equivocal.

Interpretation of possible fault or fracture zones - and perhaps zones of increased fluid saturation - raised the possibility of CO₂ leakage conduits within the lower caprock seal. Therefore, subsequent inversion and modeling studies have focused on attempts to constrain the characteristics of these features, the modes and amounts of deformation within them, and their dimensions. Because the seismic data – at least as currently processed - do not reliably resolve the sub-vertical linear features at shallower depths in the lower caprock up to and including the Hercynian Unconformity (HU), recent studies have focused in particular on determining the vertical extent of potential high permeability zones within the lower caprock.

Rucci et al. (2013) inverted two-component (quasi-vertical and quasi-EW) surface displacements derived from one ascending and one descending InSAR pair (see Rucci et al. 2013; Wright et al., 2004) spanning the 2004-2008 time interval. They found that the best-fitting solutions combined isotropic volume change and tensile opening confined to

100 m-wide, NW-striking sub-vertical zones intersecting each of the three injection wells (although they acknowledge that adding volume change within the reservoir may further improve the data fits). The combined solution for KB-502 and KB-503 yields a maximum net opening in the zone intersecting KB-502 of approximately 35 cm, or a lateral strain of 3.5×10^{-3} . The zone of significant opening (>4 cm) extends about 4 km SE-NW, and from 400-450 m above the reservoir to 300-350 m below it. The maximum cumulative dilation is much greater than the 5-6 cm in the solution of Vasco et al. (2010), but the lateral strain is similar to the 3.2×10^{-3} obtained by InSAR-constrained hydro-mechanical modeling by Rutqvist et al. (2011) using a vertical zone 50 m wide extending 200 m above the injection horizon.

Further, detailed forward modeling studies that incorporated a narrow vertical permeable zone above the KB-502 reservoir were carried out by Shi et al. (2012) and Rinaldi and Rutqvist (2013). Shi et al. (2012) concluded that tensile opening within a 4 km-long, NW-trending fracture zone (based on Vasco et al., 2010) initiated within the reservoir around November 2005. History matching of the calculated bottom hole pressure indicated that pressurization and fracture opening was confined to the reservoir interval until March 2006 and then propagated upward into the lower caprock to attain, in a scenario based on Vasco et al. (2010)) and Morris et al. (2011), a total height of 360 m within and above the C10.2 reservoir by July 2007. Although the modeling results are consistent with the development of the surface uplift pattern over time, the equivalent fracture opening through March 2006 is sub-millimeter, at least three orders of magnitude less than that estimated by Rucci et al. (2013) through 2008. However, Shi et al. (2012) argue that this estimate corresponds to only the first few months of fracture opening and also that the equivalent total aperture change would be larger if numerous fractures were involved.

Rinaldi and Rutqvist (2013) conducted time-dependent, hydro-mechanical modeling of the KB-502 injection constrained by an InSAR range-change time series covering the period 2003-2009 and the pressure and injection rate history at KB-502. Like Shi et al. (2012), Rinaldi and Rutqvist interpreted the injection rate and pressure history and the

appearance of the double lobe in the InSAR range change as evidence for sudden pressure-induced fracture opening. Based on Vasco et al. (2010) and the 3D seismic interpretation, a vertical, 3.5 km-long, NW-trending, orthotropic fracture or damage zone was activated in the lower caprock after the first five months of injection. Although they do not report changes in fracture aperture, their base model, in which an 80 m-wide fracture zone extended 350 m above the reservoir, produced good matches to the pattern of cumulative range change in the vicinity of the double lobe and to the transient evolution of the ground displacement at a point over KB-502 through the well shut-in in July 2007. A series of sensitivity tests explored the effect of varying the permeable fracture zone length, width and, in particular its height. Extending the fracture zone 700 m above the reservoir produced much larger range change amplitudes than observed, while allowing it to penetrate the HU at 900 m and connect with the shallow aquifer produced much smaller amplitudes and a poor fit to the range-change time series.

While there is a consensus among the inversion and modeling studies that overpressure and fluid penetration into the lower caprock at KB-502 was confined to a narrow zone that probably does not extend more than ~400 m above the reservoir, all of the papers acknowledge that the inversion solutions or modeling results are subject to significant uncertainties. These stem from the inherent non-uniqueness in using surface displacements to constrain sources of subsurface deformation and fluid flow. Non-uniqueness arises chiefly from tradeoffs among source location and geometry - and particularly source depth -, the mode(s) and strengths of the deformation sources (Rucci et al., 2013), flow properties (Shi et al., 2012; Rinaldi and Rutqvist, 2013), and the elastic properties of the reservoir and overburden (Vasco et al., 2010). The deformation modes can include pressure-driven isotropic volume change, tensile opening, and possibly shear displacement and shear-induced dilatation. In other words, deformation sources located at different depths and of different sizes and strengths can produce similar surface deformation patterns. Non-uniqueness can, in general, only be reduced by adding independent prior constraints on the model parameters. Consequently, the accuracy of an inverse solution or forward model depends heavily upon the known or assumed constraints.

The chief independent constraints on the location and geometry of the fault/fracture zones used in the inversions by Vasco et al. (2010) and Rucci et al. (2013) and adopted by Rutqvist et al. (2011), Shi et al. (2012) and Rinaldi and Rutqvist (2013), are the linear features identified in the 3D seismic. Vasco et al. and Rucci et al. further adjusted the lateral dimensions and dips of the fault/fracture zones to provide initial best fits to the InSAR displacements themselves, so these constraints are not entirely independent of the data and are themselves subject to tradeoffs.

Vasco et al. (2010) demonstrated that the elastic model of the reservoir and caprock can be a significant source of uncertainty in inverse and forward model solutions. They derived a 20-layer elastic model from P- and S-wave velocity logs and density profiles from several of the Krechba wells (this model was also used by Rucci et al., 2013), but available velocity logs [provided to researchers by the In Salah Joint Industrial Partnership (JIP)] are of generally poor quality above the lowermost caprock (C10.3). Furthermore, it is difficult in general to relate the dynamic estimates derived from seismic velocities to appropriate, field-scale static moduli (e.g. Fjaer, 2009; Li and Fjaer, 2012), which are therefore inherently uncertain. The same uncertainties apply to the six-layer model (Gemmer et al., 2010) used by Rutqvist et al. (2011) and Rinaldi and Rutqvist (2013).

The published deterministic inversion studies produced a single solution that provides the best fit to the data along with formal variance estimates within the known or assumed constraints on the model, and subject to the particular regularization scheme imposed to stabilize the solution. The solutions described above do not consider uncertainties in model parameters that are fixed *a priori*, and so are not able to explore alternative solutions permitted by the data. The forward models similarly arrive at best-fit solutions by trial and error. Rinaldi and Rutqvist (2013) did, however, demonstrate that end-member models provide poor fits to the observations, particularly if the fracture zone and migration of CO₂ are not confined below the HU at ~900 m depth.

In order for inversion or modeling results to be of maximum use in evaluating the performance of an injection operation and in planning future strategy, uncertainty estimates on the solutions are needed from which the reliability of the results can be assessed. Ideally, this requires a comprehensive exploration of the parameter space (i.e. both the prior constraints and the free model parameters) to describe the distribution of alternative models that are the most consistent with the data. In this study we accomplish this by using a Markov Chain-Monte Carlo (MCMC) stochastic inversion method that systematically searches the model space by sampling from uncertainty distributions on the parameters that constitute prior constraints. We first carried out forward modeling and inversions to examine the sensitivity of solutions to uncertainties in assumed prior constraints and the set-up of the inversion problem specific to the situation at In Salah. Guided by these initial studies, we then carried out stochastic inversions of the InSAR data to derive quantitative estimates of the probabilities that the pressure perturbation driven by injection into KB-502 reached different depths within the lower caprock.

2.0 INVERSION METHOD

Here we provide a general overview of the MCMC stochastic inversion method. Adaptation of the method for application to the specific inversion problem at In Salah is described in more detail in the next section.

The inverse problem can generally be described by letting D and X denote the data and model spaces, respectively. Then suppose that there exists a mapping G such that:

$$d = G(x) \quad (1)$$

The goal is to find models x_0 that correspond to the set of observations, d_0 . The range of possible solution models, X , is limited by prior knowledge.

Our implementation of MCMC is a derivative of the Metropolis-Hastings algorithm as described by Mosegaard and Tarantola (1995), and is discussed in detail by Ramirez et al. (2005). The inversion approach uses a Markov chain process to control random sampling of the model space, which is effected by proposing a large number of trial models

(realizations), x_0 . Within this framework, the solution to the inverse problem is a Bayesian estimate of the posterior probability density function (pdf) defined over the space of possible models, X . Then, for any potential solution $x_0 \in X$, the method will provide an estimate of the probability that x_0 is the true state of the underlying system.

The MCMC simulation algorithm proposes sample models according to the unknown posterior distribution. Simulated data are calculated by running each proposed model through an appropriate computational forward model to calculate a measurable quantity that corresponds to the observed data. The likelihood $L(x_0)$ that a given model $x_0 \in X$ produced the observed data is calculated based on the fit of the simulated data to the observations, subject to the prior constraints. Based upon this likelihood, an importance-sampling algorithm incorporating a randomized decision rule accepts or rejects the model for inclusion in the posterior distribution. The outcome of this decision is also used to determine how the next trial model is selected. This procedure is repeated over typically $\sim 10^5$ trials until the chains converge to a stable solution; i.e. all Markov chains are sampling from the posterior distribution. The final inverse solution is the posterior pdf over the range of the alternative models that are consistent with the measured data and prior information, which provides a comprehensive description of uncertainty. Therefore, the stochastic inversions provide quantitative estimates of the reliability and uniqueness of the solutions that can be obtained from the data and prior constraints.

MCMC is similar to deterministic inversion (e.g. Rucci et al., 2013) in that both approaches propose trial models and use a forward solver to calculate responses at the observation points that are compared with the data. However, the two approaches differ in how the trial models are updated and in the form of the final solution. Specifically, the MCMC random model generator replaces the deterministic updating scheme, and the MCMC solution is a pdf defined over the model space whereas each deterministic inversion selects a single model that best explains the data.

2.1 Adaptation of MCMC to Inversion of In Salah InSAR Data

In the case of In Salah each source model is a 3D distribution of fluid overpressures (pressure plume) induced in the subsurface by CO₂ injection. Prior knowledge is provided by the injection pressure history, the location of the injection interval, and well and geophysical data on both the locations and geometries of the reservoir and possible high permeability zones in the lower caprock and rock mechanical properties. The location of the injection interval and the injection pressure govern the generation of randomized pressure plume realizations.

The base structural model of the reservoir and caprock in the vicinity of well KB-502 is shown in Figure 3. The reservoir is modeled as a 20 m-thick layer. Based on well and seismic data (Vasco et al., 2010; Morris et al., 2011), a NW-trending, 500 m-wide vertical zone of potentially enhanced permeability intersects the reservoir and extends through the caprock to the HU at 850 m depth. The caprock, reservoir and underburden are treated as an homogeneous elastic half-space with depth-averaged moduli based on the Statoil six-layer reference model as presented in Rinaldi et al. (2013, Table 2).

Figure 4 shows the computational steps in the MCMC procedure as adapted for In Salah inversions. Realizations of 3D pressure plumes are built within the structural model from one or more contiguous ellipsoids (Figure 4, step A). The ellipsoids represent either zones of isotropic volumetric inflation/deflation or, by constraining one axis of the ellipsoid to be very small, deformation of planar fracture-like sources. The ellipsoids can rotate about any axis, translate, change size and ellipticity and change pressure from one trial source configuration to the next. The number of ellipsoids in a given plume and the overpressure values assigned to each ellipsoid can change from iteration to iteration. Each ellipsoid is mapped to a set of nodes in the 3D inversion grid, and each node is treated as a point pressure-driven deformation source within the plume.

At least one of the ellipsoids in a proposed overpressure plume is connected to the injection interval within a given injection well. To ensure that the number of degrees of

freedom remains constrained, all of the grid cells in each ellipsoid are assigned a discrete category value representing fluid overpressure at each iteration. For example, if the set of category values for overpressure is $\{A, B, C\}$, then: $A \rightarrow \Delta P_1, B \rightarrow \Delta P_2, C \rightarrow \Delta P_3$, where the ΔP_i represent discrete, non-zero overpressure values assigned to grid nodes located within an ellipsoid. The remaining grid nodes are assigned zero overpressure. The maximum allowable overpressure is the injection bottom hole pressure.

Point deformation sources can be isotropic volume changes (henceforth referred to as dilatational sources) or tensional opening/closing (Mode I). In general, isotropic volume change is more likely in porous media such as the reservoir layer and tensional opening/closing more likely in fault or fracture zones. We did not include pressure-activated shear sources because the trend of the fault/fracture zone suggested by the seismic and InSAR data is NW, along the direction of maximum horizontal compressive stress, and therefore as a whole is not favorably oriented for shear activation. It is conceivable, however, that the zone contains *en echelon* arrays of small faults or fractures that are favorably oriented for shear activation, so this model could be investigated in a future study.

The mode of deformation assigned to each point source depends on its location on the grid. Arbitrarily-shaped inversion grid sectors are specified, each of which is assigned a specific deformation mode. For example, we could specify that point sources located within the horizontal reservoir layer are dilatational and, if the pressure plume extends within an enhanced permeability zone into the caprock, those within the zone are tensional. The strikes and dips of tensional sources can be fixed at user-specified values or can vary according to the orientation of the ellipsoids within which they are located.

An initial decision to accept or reject a pressure realization is based on the consistency of the proposed model with the base model (Figure 4, step B). In the base model it is assumed *a priori* that pressure changes have a high probability of occurring in the reservoir, a moderate probability of occurring in the potential vertical fault/fracture zone, and a very low probability of occurring elsewhere. Figure 3 illustrates how these

probabilities are represented on the computational grid. Grid nodes that have a non-zero probability of experiencing pressure changes as a result of injection are shown in either green or red, and zero-probability nodes are rendered transparent. For example, in the model shown pressure changes are twice as likely to occur within the reservoir horizon (red nodes) than within the vertical fracture zone (green nodes). Proposed pressure plumes that encompass transparent nodes are penalized whereas models that encompass green or red nodes are encouraged.

The accept/reject decision employs the Metropolis-Hastings algorithm mentioned above using likelihoods calculated from the fit of the proposed realization to the node probabilities in the base model. Grid nodes having non-zero overpressure in the realization are assigned a value of 1 while all other nodes are set to zero. The likelihood is calculated by comparing these node values to the corresponding base model node probabilities. Proposals that are fully contained within the base structural model yield the largest likelihoods, the likelihood falling off in proportion to the fraction of the model realization that falls outside the base model. If the current proposal is rejected, then the inversion process reverts back to step A, where a new realization is generated by perturbing the last trial to be accepted according to a randomized rule (see Ramirez et al., 2005). If the proposal is accepted, synthetic InSAR data are calculated at the surface observation points by summing the displacements generated by the pressure-driven point deformation sources according to the deformation modes assigned to each node. The elastic moduli used in these calculations are randomly sampled from a prior distribution. The forward calculations are carried out using the Lawrence Livermore National Laboratory (LLNL) code SYNEF (unpublished), which computes displacements, tilts, strains and stresses throughout a 3D linear elastic half-space employing, in the present case, Green's functions derived by Okada (1985, 1992) for dislocations embedded in an homogeneous elastic half-space. Both InSAR line-of-sight range change and quasi-vertical and quasi-EW displacement components can be calculated, given the SAR acquisition geometry (see Rucci et al., 2013).

Both isotropic volume change and Mode I opening are calculated from pressure change without considering poroelastic effects. Mode I displacements are derived approximately from the opening of an equivalent pressurized elliptical crack having the same surface area and internal volume as the dislocation. The opening displacement (i.e. relative displacement of the two walls) of a flat elliptical crack lying in the $z=0$ plane under uniform internal pressure is given by (Green and Sneddon, 1949; Mura, 1987))

$$u_z(x,y) = \frac{2(1-\nu)}{\mu} \frac{b}{E(k)} \left[1 - \frac{x^2}{a^2} - \frac{y^2}{b^2} \right]^{\frac{1}{2}} p \quad (2)$$

where a and b are the semi-major and –minor axes of the ellipse, respectively, ν Poisson’s ratio, μ the shear modulus, p the pressure, and $E(k)$ a complete elliptical integral of the second kind. The opening is elliptical with maximum displacement at $(x,y) = (0,0)$ given by

$$u_z^0 = \frac{2(1-\nu)}{\mu} \frac{b}{E(k)} p \quad (3)$$

The uniform opening of the equivalent dislocation can then be calculated as

$$u_z^d = \frac{2}{3} u_z^0 \quad (4)$$

The same procedure as in step D (Figure 4) is employed in the final decision to accept or reject a realization based on a likelihood calculated from the fit of the synthetic InSAR data to the observations (Figure 4, steps F and G). Proposed pressure models accepted at this stage become part of the posterior distribution.

3.0 APPLICATION TO IN SALAH

We use MCMC to systematically assess uncertainties in inverting InSAR-derived surface displacements to map the evolution of the pressure distribution from injection at In Salah well KB-502. Our primary focus is on assessing factors that influence the vertical resolution attainable with the available data and prior constraints. The study is conducted in three parts: (1) Sensitivity analyses using synthetic reservoir and caprock models to represent likely reservoir scenarios; (2) stochastic inversion of synthetic data to evaluate

the impacts of various sources of uncertainty; and (3) stochastic inversions of field data to estimate the probabilities that the pressure plume penetrated to different depths within the caprock and to different distances laterally within and above the reservoir.

3.1 Synthetic models

3.1.1 Sensitivity Analyses using Candidate In Salah Scenarios

As discussed in the Introduction, the ability of InSAR data to resolve the extent of overpressure or fluid penetration into the lower caprock above the In Salah reservoir is inherently limited, but supplying additional prior constraints on the inverse problem can reduce the trade-offs responsible for non-uniqueness and hence improve vertical resolution. In the simple synthetic analyses described here we examine the sensitivity of surface displacement patterns and amplitudes to prior constraints on the characteristics and distributions of deformation sources and overburden properties in order to evaluate their potential effectiveness in reducing non-uniqueness in inverse solutions. The surface displacement patterns were calculated using analytic Green's function solutions implemented in the SYNEF code described earlier..

We consider first the sensitivity of surface displacements to selection of the deformation modes that characterize different parts of the overall plumbing system. As argued earlier, the two most likely modes of deformation resulting from injection at In Salah are volumetric dilatation and tensional opening in Mode I. Dilatation is commonly associated with fluid flow through porous media, while Mode I opening occurs when increased fluid pressure forces apart the opposite faces of fractures and faults (i.e. the displacement is normal to the fracture plane). Therefore, likely In Salah scenarios are those that include dilatational deformation within the relatively permeable C10.2 reservoir together with fracture opening within the vertical zone interpreted from the 3D seismic data. Although both modes of deformation may occur both within the reservoir and caprock (e.g. Shi et al., 2012; Rucci et al., 2013), we examine cases in which only one deformation mode is active in each zone. Our objective is to evaluate whether changes in the InSAR pattern resulting from the different scenarios are sufficiently distinctive to discriminate between the scenarios, and particularly to resolve the height of

the pressure perturbation above the reservoir. We also examine the sensitivity to overburden elastic properties, and evaluate the resolving power of two-component displacement data compared with scalar LOS range changes.

3.12 Distribution of Dilatational and Opening-mode Deformation Sources

Figure 5 shows plan and perspective views of the three synthetic models used for this study. The green and pink elements indicate the pressurized region in the reservoir and caprock fracture zone, respectively. Model 1 assumes that the over-pressurized zone is fully contained within the reservoir, so that only green elements contribute to the deformation field. Models 2 and 3 assume that the over pressured zone extends from the reservoir 300 m and 940 m into the lower caprock, respectively, so that green and pink elements both contribute to the deformation.

Figure 6A shows InSAR LOS displacements calculated from Models 1 to 3 for a deformation scenario in which the mode of deformation in both the reservoir and caprock is dilatational. The three panels show how the surface range-change pattern varies as the overpressurized zone migrates upwards from the reservoir into the lower caprock. The pattern becomes more elongated SE-NW as the pressure plume migrates upwards along the fracture zone, and range change amplitudes increase significantly. Since there is only a modest change in the InSAR pattern, particularly between Models 1 and 2, the primary indicator of upward pressure migration when only dilatation drives the deformation is an increase in the overall amplitude of the InSAR signal. However, higher amplitudes could also be produced by increasing the reservoir pressure without significant migration up the fracture zone, and this tradeoff degrades the ability to resolve the vertical extent of the plume.

Figure 6B corresponds to a scenario that has only opening-mode sources in both the reservoir and damage zone. All three synthetics exhibit the double-lobed pattern seen in the InSAR LOS data above KB-502 (Vasco et al. 2010), showing that such a double-lobe pattern can be created even by areally distributed Mode I sources confined to the

reservoir layer. Even though the maximum amplitude increases (in these synthetics) from 0.3 mm to 5 mm, the change in the displacement pattern as the pressure anomaly migrates upwards into the lower caprock is relatively slight. Therefore, the same tradeoff between overpressure and depth applies to this scenario as to the first, suggesting that in general it would be difficult to resolve the pressure plume's vertical extent when the same mode of deformation occurs within both the reservoir and damage zone.

The third scenario (Figure 6C) has only dilation in the reservoir and fracture opening within the lower caprock damage zone. This is the same basic model as that used by Vasco et al. (2010). In this case there are significant changes in the range-change pattern as the pressure anomaly migrates upwards into the lower caprock, even though the amplitude changes are relatively small. The changes in the LOS displacement pattern are less likely to be produced by tradeoffs between overpressure magnitude and caprock penetration, which suggests that in this dual-source scenario the InSAR data can provide improved constraint on the vertical extent of a pressure perturbation.

Figure 7 compares the observed range change above KB-502 between March and July 2007 with synthetics calculated from dual-source and opening-mode only scenarios. All three images show double lobed patterns having similar orientations. However, the dual-source scenario produces an InSAR image that is most similar in both its pattern and amplitude to the observations, while the opening-mode only scenario produces a subsidence trough that is not present in the real data. These comparisons suggest that the combination of dilatational and opening-mode sources described above is one model that is compatible with the observations, in which case the InSAR data should provide a modest degree of constraint on the pressure distribution at depth.

3.13 Sensitivity to Elastic Properties

The sensitivity of surface displacements to the elastic property model is illustrated in Figure 8. The curves show LOS displacement profiles along the transect line indicated by the white dashed line in Figure 7. The left profile plots displacements for the three

pressure distribution models using the dual-source scenario. Note that the maximum difference between the curves is approximately 4 mm. The plot on the right shows three curves all calculated using the model having pressure penetrating 300 m above the reservoir, but with different values of the half-space shear modulus. The center curve corresponds to the base half-space elastic model (shear modulus 3.38 GPa); the bottom and top curves were calculated using shear modulus values double and half the base value, respectively. The maximum difference between the upper and middle curves is similar to the difference between the curves for the different models. This demonstrates that relatively modest changes in the assumed elastic moduli introduce significant uncertainties in calculated surface displacement amplitudes that can result in tradeoffs with the depths of pressure perturbations. Uncertain poroelastic properties can also affect surface displacement estimates but their effects were not evaluated in this study.

3.14 Two-component Displacement Data

Figure 9 shows the quasi-vertical and quasi-horizontal displacements generated by Models 1 to 3 assuming the dual-source scenario. The quasi-vertical displacements are similar to the range changes shown in Figure 6. The horizontal displacement pattern progressively rotates as the pressure perturbation penetrates to shallower depths, but the difference between the Model 1 and 2 patterns is subtle. However, even though the horizontal displacements produced by the given source geometry are less sensitive to the height of the pressure plume, they add independent information to the inversion and therefore hold some potential to improve vertical resolution.

In summary, the synthetic forward modeling described above leads to the following general conclusions: (1) Dual-mode models that combine dilatational source restricted to the horizontal reservoir with opening-mode sources restricted to a narrow tabular zone in the caprock produce surface displacements that are most compatible with the InSAR observations on the vicinity of KB-502, and therefore have potentially greater power to resolve the vertical extent of pressure plumes. Conversely, it is difficult to discriminate between the heights of pressure perturbations when only one mode of deformation occurs

in both the reservoir and the vertical zone; (2) uncertainties in elastic properties introduce trade-offs that degrade the ability to resolve (in any inversion approach) the vertical extent of a pressure plume; and (3) two-component displacement data hold some potential for improving vertical resolution beyond that attainable with InSAR scalar range changes. We further examine each of these factors in the following section by carrying out MCMC inversions of the data calculated using the synthetic models.

3.2 Stochastic Inversions of Synthetic Data

We carried out inversions of synthetic data to evaluate the impact of various sources of uncertainty on the resolution of overpressure migration into the lower caprock. The inversion domain encompasses the same volume as shown in Figure 3, and is discretized into 30 x 25 x 50 grid cells in E, N and depth respectively (node spacing 200m x 200m x 20 m). For these inversions, we assume that the elastic properties of the reservoir and caprock are uncertain, so at each iteration the shear modulus value is sampled from a uniform distribution between 3.00 and 3.76 GPa, centered on the base value of 3.38 GPa used to generate the synthetic data. The Poisson ratio is likewise sampled from a uniform distribution between 0.27 and 0.285. The strike and dip of all opening fractures are fixed at 315° and 90°, respectively.

The models produced by the inversion contain pressure perturbation amplitudes distributed in 3D space. However, our main goal in this study was to estimate the probability of pressure leakage. Thus, we chose to post-process the pressure models in the posterior distribution to calculate the probability of pressure leakage away from the reservoir and the images presented show probabilities rather than pressure. Alternatively, one could use the pressure perturbation models to estimate the state (opening or closing) of the fracture(s) and the contribution of fracture opening to the surface deformation.

The posterior pdf (solution) obtained from each inversion contains between 45,000 and 90,000 models. Each inversion used eight compute cores running for about 16 hours. To carry out the resolution assessments we calculated two simple probability measures. In

the first of these, we selected the top 3% of the models in each pdf that best fit the data and used this subset to estimate a measure of the probability that a pressure perturbation is present at each node in the grid. These estimates are determined by counting the number of models, m_n that have non-zero pressure within each grid cell. The probability measure is estimated simply by normalizing the counter value for each cell by the maximum counter value. In other words, the probability that a pressure perturbation is present within the cell having the greatest counter value is assumed to be 1.0, and the probability measures for all the other cells are calculated relative to that cell.

Figure 10 shows the probabilities obtained by inverting synthetic LOS data from Models 1 to 3 and using the dual-source scenario. The horizontal slices at reservoir level show that cells having non-zero probabilities are largely confined within the lateral boundaries of each model. Vertical smearing of the pressure perturbation is evident in the vertical sections for Model 1 and 2, with probabilities greater than ~ 0.7 concentrated within the vertical fracture zone, above the reservoir. These results indicate that we can expect the horizontal resolution attainable by inversion of InSAR data to be significantly better than the vertical resolution. However, for these representative synthetic cases, cells having probabilities greater than 0.5 do not extend vertically more than about 200 m above the upper boundaries of the two models, showing that the vertical resolution is only moderately degraded. Similar results (not shown) are obtained for purely dilatational synthetic models, but in these cases the cells having the highest probabilities are systematically located above the reservoir layer and the solution for Model 1 is smeared to a significantly greater height than in the dual-source case.

Results of inverting synthetic quasi-EW and quasi-vertical displacements are shown in Figure 11. While these results reinforce the main conclusion that the resolution in the solutions is better horizontally than vertically, it is perhaps surprising that, given the additional information provided by the quasi-EW component, the vertical resolution is significantly worse than that obtained from the equivalent LOS displacements, especially above the top of Model 2. At present, we have not ascertained the cause of this.

The second probability measure employed estimates the probability that a pressure perturbation extends to a given depth within the lower caprock, regardless of where that occurs in the 3D grid. For this estimate the top 3% of the models in the posterior pdf that best fit the data are again used. The number of nodes at each depth having non-zero overpressure is counted and then normalized to the count for the reservoir level. Therefore, the probability of a pressure perturbation at reservoir depth is 1.0, and the probabilities at other depths are estimated relative to the reservoir. The resulting plot of this probability measure as a function of depth provides a better vertical resolution metric – and one that is easier to visualize - than the slices shown in Figures 10 and 11 because all of the nodes at each depth contribute to a single probability estimate. Plots of this second probability measure are shown in Figure 12.

Figure 12A shows the probabilities estimated for an inversion of synthetic LOS data generated using the dual-source scenario. If the vertical resolution were perfect, the curve for Model 1 (blue) would look like a delta function with probability 1.0 at the reservoir depth and zero elsewhere (this also applies to panels B-D). In fact, the probability at the reservoir depth is 1.0 but non-zero at shallower depths; for example, there is a probability of 0.6 that the plume extends to 1700 m depth, indicating somewhat limited resolution, but a probability of only 0.1 that it extends to 1500 m and zero probability that it extends to the HU. The Model 2 result (green) gives the probability of the pressure perturbation being confined below 1500 m as 0.5, but the probability that it reaches 1100 m is less than 0.05. For Model 3 (red) the probability of the plume reaching depths as shallow as 950 m is 0.9 or higher, and 0.75 that it reaches the HU.

The probability curves in Figure 12B result from inversion of range changes using only dilatational sources. The vertical resolution for Models 1 and 2 is significantly poorer than achieved with the dual-source scenario. For example, the solution for Model 1 has a probability of 0.6 that the pressure perturbation reaches a depth of 1600 m, compared with 0.25 for the dual-source scenario. While the probability that in the Model 2 solution the pressure perturbation is present at 1500 m - the correct upper limit - is much higher

than seen in Figure 12A, the pressure distribution is smeared vertically, resulting in much higher probabilities also at depths as shallow as 1300 m.

Figure 12C shows the probabilities resulting from an inversion of two-component displacements using the dual-source scenario. Comparing with Figure 12A, we see that the blue and red curves are similar, suggesting that range change and two-component data yield comparable vertical resolution for Models 1 and 3. In contrast, the curve for Model 2 is similar to that in Figure 12B above 1500 m, again indicating degraded vertical resolution above this depth compared with the LOS solution in 12A and consistent with the interpretation of Figure 11. However, the separation between the depths corresponding to the highest probabilities (say above 0.75) is wider in Figure 12C, which suggests that inversions of two-component data may be more effective in discriminating between a pressure perturbation that is confined to the reservoir from one that extends a few hundred meters above it.

These synthetic results strongly suggest that inversions of either scalar range change or two-component displacement data should be capable of distinguishing a pressure perturbation that approaches the HU from one contained below a depth of ~1500 m, and probably even 100-200 m shallower. While the solutions derived for Models 1 and 2 are distinct in these noise-free synthetic cases, the vertical resolution attainable with real data is likely to be degraded so that it is less certain whether it will be possible to discriminate between pressure perturbations that extend to different heights within the lower caprock below a depth of about 1500 m. The results also suggest that two-component displacements derived from InSAR may improve vertical resolution to some extent; however, this conclusion is less than definitive, which may be consistent with the relatively low sensitivity of horizontal displacement patterns to the different source models (Figure 9). Finally, base models that include both opening-mode and dilatational sources appear to be more effective in resolving the vertical extent of a pressure plume.

Considering the uncertainty in deriving elastic properties for In Salah discussed in the Introduction, the $\pm 11\%$ variation in shear modulus assumed so far in inverting the

synthetic data is probably overly optimistic. Figure 12D shows the results of carrying out the same inversion used to produce Figure 12C but sampling the shear modulus from a uniform distribution between 1.69 and 6.76 GPa (-50% to +100%), which is probably more realistic. These inversions also allowed random (uniform) variation in Poisson's ratio in the range 0.27 – 0.285. The probability curves for Models 1 and 3 are fairly similar to those in Figure 12C. The curves for Model 2 are markedly different; the effect of the greater uncertainty is to flatten the curve so that the Model 1 and Model 2 curves are much closer together (this is probably true in general for the entire range of probabilities, as the steps at probability values of 0.45 and 0.75 are likely sampling artifacts in this particular inversion). This suggests that it would be quite difficult to discriminate between Models 1 and 2 given a large uncertainty in elastic properties. However, even given an uncertainty as large as this, it should still be relatively easy to discriminate both of the other models from Model 3.

4.0 STOCHASTIC INVERSIONS OF IN SALAH FIELD DATA

We inverted subsets of the In Salah InSAR data set over three time intervals beginning at the inception of injection at well KB-502 in August 2005 and ending in August 2010. We focused on the response to injection in KB-502 in order to provide a basis for assessing the likelihood that the CO₂ plume penetrated above the storage volume into the lower caprock, and, if so, the likely vertical extent of penetration. Since the inversions of InSAR data constrain only changes in the fluid pressure or volume distribution in the subsurface, they can provide information about the horizontal and vertical extents of pressure perturbations that can be used indirectly, for example as constraints on flow modeling, to investigate the distribution of actual CO₂ saturation.

The time periods covered by the three InSAR data sets are shown relative to the KB-502 injection history in Figure 13. All of the InSAR data, shown in Figure 14, were

processed by TRE and made available by the JIP. The data sets covering the time intervals June 2005-August 2006, during the first phase of injection, and December 2007-June 2008, during shut-in, comprise the Envisat C-band permanent scatterer (Ferretti et al., 2001) range change data described by Vasco et al. (2008, 2010). The estimated standard deviation of these data is in the range 1.0-2.5 mm (Rucci et al., 2010, 2013). The third data set covers the time interval November 2009-July 2010 during the second injection phase, and comprises quasi-EW and quasi-vertical displacements derived from ascending and descending Cosmo-SkyMed (X-band) interferograms processed using TRE's SqueeSARTM method, which integrates information from both permanent and distributed scatterers (Ferretti et al., 2011). Rucci et al. (2013) describe the method used to extract the two displacement components (from Envisat data in their case). The standard deviations of the Cosmo-SkyMed displacement measurements are estimated to be less than 3 mm (A, Rucci, TRE, personal communication). The range-change and two-component displacement data were both re-sampled on to 100 m x 100 m grids.

4.1 Model Set-up and Choice of Constraints

We used the insights developed from the synthetic data inversions to guide the inversions of the field data. The 3D inversion domain and grid are identical to those described above. We first experimented with different inversion constraints and inversion set-ups (i.e. the way pressure models are sampled) to evaluate their impacts on pressure perturbation probability estimates.

Preliminary work (J. White, LLNL, personal communication) had indicated that the Gemmer et al. (2012) reference model may overestimate the caprock stiffness, and that a uniform reduction by a factor of 0.5 appeared to provide a better fit to observed range-change amplitudes. Metrics generated as part of the MCMC procedure also indicted that the lower stiffness values produced better fits to the data. Therefore, in the inversions discussed below the shear modulus was sampled from a uniform distribution between 0.3 and 2.0 GPa.

Figure 15 shows probability estimates derived from the June 2005 – August 2006 range-change data using various model set-ups. The curves indicate that the probability that the pressure perturbation reached the HU is 10% or less regardless of the assumed constraints, and the probabilities estimated from all of the solutions fall off rapidly across the bottom 400 m of the caprock (depth range 1400 – 1800 m). The results of inversions that employed the dual-source scenario and six ellipsoids to represent the overpressure distribution (green and blue curves) have a probability of about 0.5 that the pressure perturbation is present at the Hot Shale (depth 1500 m), falling to 0.3 at 1400 m. The inversion employing only dilatational sources (dashed curve) results in a probability of 0.25 at 1500 m.

In one of the trial inversions (solid blue line) the strike and dip of opening-mode sources were randomly sampled from uniform distributions over the ranges $\pm 180^\circ$ and $\pm 90^\circ$, respectively. The opening-mode strike and dips for all models in the posterior pdf are plotted in Figure 16. The two predominant modes in the strike histogram at about 130° and 300° - 325° are in close agreement with the predominant fracture strike orientations found by Iding and Ringrose (2010) from analysis of core and image logs from KB-502. Iding and Ringrose reported that fractures are dominantly sub-vertical, which we interpret as dips in the range 75° - 90° . This range encompasses the two predominant peaks in the dip histogram. The predominant strikes and dips recovered by the stochastic inversion are also in reasonable agreement with those found by Rucci et al. (2013) to provide an optimal fit to the InSAR data. Therefore, we judged it valid to constrain the strike and dip used in the inversion to be 318° and 90° , respectively, in order to reduce the number of degrees of freedom and trade-offs that might limit resolution. The probabilities that result from applying these constraints are shown by the green curve in Figure 15.

The most significant differences remaining after applying the geometrical constraints are the pressure perturbation probabilities at depths between 1300 m and 1550 m. Given the apparently poorer vertical resolution obtained using only dilatational sources in the synthetic tests, we elected to use the dual-mode scenario for the final inversions of the In Salah data. Significant differences in the probabilities within the same depth range also

result from using a maximum of six compared with a maximum of three ellipsoids to represent overpressure distributions. We chose to allow the inversions to use up to six ellipsoids to provide better spatial sampling of pressures.

4.2 In Salah Inversions for Three Time Periods

Figure 17 shows probabilities that a pressure perturbation exists according to the first probability measure described previously, calculated from the inverse solutions for the three time periods defined in Figure 13. The top row in Figure 17 shows horizontal slices at the reservoir level and the bottom row vertical slices along W-E transects for each time period. Figure 18 shows probabilities that a pressure perturbation exists as a function of depth (second probability measure) for the three periods. The blue curves result from inversions that sample from a shear modulus range (2-7 GPa) that is representative of the Gemmer et al. (2012) reference model, and are included for comparison with the preferred range of 0.3-2.0 GPa.

The horizontal probability distribution for the 2005-2006 time period (Figure 17 top left) during the initial injection images a narrow NW-trending zone intersecting the horizontal injection interval of KB-502. The area defined by probabilities greater than 0.5, corresponding to locations where the pressure perturbation is relatively well resolved, is approximately 3 km long and 1 km wide, although the area of non-zero probability extends about 3 km NW and 1 km SE of the well, respectively. The zone of highest probability (0.75-1.0), corresponding to the highest resolution, is centered approximately 1.5 km NW of the well and is two grid cells (400 m) wide. In Figure 18, this high-probability zone is confined within the lowest 150 m of the caprock, but there is a probability of ~0.5 that the pressure perturbation extends upwards a further 150 m to reach the Hot Shale. This result is in closely consistent with the fracture opening solution of Vasco et al. (2010) and is also consistent with that of Rucci et al. (2013), although the maximum fracture aperture opening in the latter solution is located only about 300 m NW of the well. The probability that the pressure perturbation approaches within 150 m of

the HU is less than 0.15. Comparison of the green and blue curves indicates only a small sensitivity above a depth of 1400 m to the assumed elastic properties.

The second set of probability plots correspond to a six-month snapshot of the negative pressure changes that developed during the shut-in interval. While there a slight suggestion of pressure change NW of KB-502, the high probabilities in the solution are tightly restricted to a small zone immediately SE of the well and within the lowest 100-200 m of caprock. This suggests that if the mechanism for fluid migration during injection was indeed increased permeability owing to pressure-induced fracture opening and/or hydrofracture, then closing of fractures in the lowermost caprock after shut-in may have reversed the permeability change, thus allowing elevated pressures at shallower depths to be maintained. In this case, pressure dissipation would only take place within the relatively porous reservoir, resulting in the slowing decline of the wellhead pressure seen in Figure 13, and the slow rate of surface subsidence observed in the InSAR data.

The amplitudes of surface displacements imaged during the second injection phase are a factor of 4-5 smaller than the range changes observed during the first phase (Figure 14). This is presumably a result of the lower overall injection pressures and rates during the second phase compared with those during the selected time interval during the first (Figure 13), although this is not clear. The reduction in signal-to-noise ratio results in overall poorer resolution in the inversion solutions, and hence the relatively low probability estimates seen in Figure 17.

The relatively high (> 0.3) probabilities in Figure 17 indicate that during the 9-month period beginning at the start of the second injection in November 2009 positive pressure changes were confined to two small zones, one in the vicinity of the toe of KB-502 and an entirely new one west of the well. Patchy pressure changes within the zone NW of the well predominantly associated with first phase of injection are imaged only with very low probabilities. Figure 18 shows that, using the preferred (lower) range of shear moduli, the highest probability of the presence of a pressure perturbation extends 100 m above the top of the reservoir. During this phase the estimated probability that the perturbation is

present at the Hot Shale is 0.6, significantly higher than during the initial injection, and there is a relatively high probability (0.4) that the perturbation extended to a depth of 1400 m. This is consistent with re-opening of pre-existing fractures after injection resumed. The probability of pressure changes above 1200 m remains low (<0.15). In this case there is a wide separation between the curves above 1500 m corresponding to the inversions using the different elastic models, and hence increased overall uncertainty in the inverse solutions. This increased sensitivity is likely a result of the relatively low signal-to-noise ratio of the data.

5.0 CONCLUSIONS

Maps of InSAR line-of-sight range changes and displacements derived from synthetic aperture data collected over In Salah during two injection phases and the intervening interval have provided one of the most important data sets used in investigating the migration of CO₂ and other fluids within the storage complex and possibly into the overlying lower caprock. In particular, inversion and forward modeling constrained by these data provide evidence suggesting that changes in fluid pressure and CO₂ saturation extended to some height above the reservoir within a narrow, sub-vertical high-permeability zone. However, the vertical extent of the pressure perturbation - and hence the height of the CO₂ plume - remains a matter of debate because it is poorly resolved by results published to date. This stems from tradeoffs inherent in modeling surface displacements produced by subsurface deformation sources when the (assumed known) parameters used as prior constraints are uncertain.

We carried out a series of systematic studies to further evaluate parameter sensitivity and sources of non-uniqueness given the InSAR data set and inversion/modeling constraints and their uncertainties specific to the In Salah operation. The primary objective of the study was to place probabilistic bounds on the vertical extent of the pressure perturbation during each phase of injection at well KB-502. To this end, we carried out stochastic inversions of both synthetic and field data that produce as solutions probability density

functions over the space of alternative models that are consistent with the data and with the prior constraints. Each inversion run used 8 compute cores running for 16 hours.

Synthetic forward modeling and inversions indicated that, of those tested, the most likely subsurface deformation scenario to apply to In Salah is one in which dilatational (isotropic inflation/deflation) sources and tensional opening/closing of fractures (Mode I) are confined to the reservoir and the sub-vertical tabular zone above the reservoir inferred from 3D seismic, respectively. This combination also yields the best vertical resolution in inverse solutions. The most robust conclusion from the synthetic study is that inversions of the In Salah data should be easily capable of discriminating pressure perturbations that approach the top of the lower caprock at the Hercynian Unconformity from those that are confined below a depth of 1400-1500 m. The synthetic results also suggest that there is a moderate chance of discriminating a perturbation at ~1500 m from one confined to the vicinity of the reservoir, but this conclusion is less certain given the present large uncertainties in elastic properties (and noisy data).

We carried out stochastic inversions of the In Salah field data using the inversion set-up and set of optimal prior constraints deduced from the synthetic study and initial application to the data themselves. From the probability solution for the first injection phase we can conclude with a high degree of confidence that pressure change was confined to a well-defined NW-trending zone intersecting KB-502 and was concentrated to the NW of the well, and that it is very unlikely that a pressure perturbation approached within 150 m of the Hercynian. There is a high probability that the pressure change extended into the lowest 150 m of the caprock, and moderate (50%) probability that reached as far as 1500m depth. These results are closely consistent with recently published deterministic inverse solutions.

The inversions also provide interesting information about the pressure distributions during the 2007-2009 well shut-in and during the second injection phase. The spatial probability distribution indicates that depressurization over a 6-month period beginning six months after shut in was tightly restricted to a small zone SE of the well and, at a 50%

probability level, extending ~200 m above the reservoir. During the first eight months of the second injection, elevated pressures appear to have been confined to two small zones, one at the toe of the well and the other 1-2 km to the west. In this case, the maximum probability of a pressure-perturbation extends 100-200 m above the reservoir and there is a 60%-70% probability that it reaches the Hot Shale. Although the relatively low signal-to-noise ratio of the data reduces the reliability of the inverse solution, we believe that there it is still very unlikely that the pressure change approached the HU during this time interval. The inversion results for both of these later time intervals may shed further light on the mechanics of permeability creation and subsequent flow in the lower caprock and reservoir.

Acknowledgements

The authors would like to acknowledge the sponsor organizations that supported this work: The In Salah Joint Industrial Partnership (JIP; BP, Statoil, and Sonatrach), and the U. S. Department of Energy, Fossil Energy Program. The JIP also provided data used in our analysis. We would like to thank in particular Iain Wright, Allan Mathieson and Rob Bissell of BP and Phil Ringrose of Statoil. We are also grateful for the InSAR data processed by Tele-Rilevamento Europa and made available, along with other data sets, by the JIP. Helpful discussions with Don Vasco (Lawrence Berkeley National Laboratory) and Josh White (Lawrence Livermore National Laboratory) helped us improve our deformation modeling approach. This work performed under the auspices of the U.S. Department of Energy by Lawrence Livermore National Laboratory under Contract DE-AC52-07NA27344.

REFERENCES

- Burgmann, R., P. Rosen, and E.J. Fielding (2000), Synthetic aperture radar Interferometry to measure Earth's surface topography and its deformation, *Ann. Rev. Earth. Planet. Sci.*, **28**, 169-209.
- Davis, E., (2011), Analysis of surface deformation at the In Salah CO₂ sequestration project, in *Proc. 10th Ann. Conf. on Carbon Capture and Sequestration*, Pittsburgh, PA, May 2-5.
- Ferretti, A., C. Prati, and F. Rocca (2001), Permanent scatterers in SAR interferometry, *IEEE Trans. Geosci. Remote Sens.*, **39**, 8 –20.
- Ferretti, A., A. Fumagalli, F. Novali, C. Prati, F. Rocca, and A. Rucci (2011) A new algorithm for processing interferometric data-stacks: SqueeSAR *IEEE Trans. Geosci. Remote Sens.*, **49**, 3460–3470.
- Fjaer, E. (2009), Static and dynamic moduli of weak sandstone, *Geophysics*, **74**, WA103-WA112.
- Gemmer, L, O. Hansen, M. Iding, S. Leary, and P. Ringrose (2012), Geomechanical response to CO₂ injection at Krechba, In Salah, Algeria, *First Break*, **30**, 79-84.
- Gibson-Poole, C. M., and S. Raikes (2010), Enhanced understanding of CO₂ storage at Krechba from 3D seismic, in *Proc. 9th Ann. Conf. on Carbon Capture and Sequestration*, Pittsburgh, PA, May 10-13.
- Green, A., and I. Sneddon (1950), The distribution of stress in the neighborhood of a flat elliptical crack in an elastic solid, *Math. Proc. Cambs. Phil. Soc.*, **46**, 159-163.
- Iding, M., and P. Ringrose, (2010) Evaluating the impact of fractures on the performance

- of the In Salah CO₂ storage site, *Int. J. Greenhouse Gas Control*, **4**, 242 – 248.
- Li, L., and E. Fjaer, Modeling of stress-dependent static and dynamic moduli of weak sandstones (2012), *J. Geophys. Res.*, **117**, B05206, doi:10.1029/2011JB009019.
- Metropolis, N., A. Rosenbluth, M. Rosenbluth, A. Teller, and E. Teller (1953), Equation of state calculations by fast computing machines, *J. Chem. Phys.*, **1**, no. 6, 1087-1092.
- Morris, J.P., Y. Hao, W. Foxall, and W. McNab (2011), A study of injection-induced mechanical deformation at the In Salah CO₂ storage project, *Int. J. Greenhouse Gas Control*, **5**, 270-280.
- Mosegaard, K., and A. Tarantola (1995), Monte Carlo sampling of solutions to inverse problems, *J. Geophys. Res.*, **100**, 12431-12447.
- Mura, T. (1987), *Micromechanics of Defects in Solids*, 2nd Ed., Kluwer, Dordrecht, Netherlands, 587p.
- Okada, Y. (1985), Surface deformation due to shear and tensile faults in a half-space, *Bull. Seismol. Soc. Am.*, **75**, 1135-1154.
- Okada, Y. (1992), Internal deformation due to shear and tensile faults in a half-space, *Bull. Seismol. Soc. Am.*, **82**, 1018-1040.
- Onuma, T. and S. Ohkawa (2009), Detection of surface deformation related with CO₂ injection by DInSAR at In Salah, Algeria, *Energy Procedia*, **1**, 2177-2184,
- Onuma, T., K. Okada, and A. Otsubo, 2011, Time series analysis of surface deformation related with CO₂ injection by satellite-borne SAR Interferometry at In Salah, Algeria, *Energy Procedia*, **4**, 3428-3434.

- Ramirez, A, J. Nitao, W. Hanley, R. Aines, R. Glaser, S. Sengupta, K. Dyer, T. Hickling, and W. Daily (2005), Stochastic Inversion of Electrical Resistivity Changes Using a Markov Chain, Monte Carlo Approach, *J. Geophys. Res.*, **110**, B02101, doi:10.1029/2004JB003449.
- Rinaldi, A. P., and J. Rutqvist (2013), Modeling of deep fracture zone opening and transient ground surface uplift at KB-502 injection well, In Salah, Algeria, *Int. J. Greenhouse Gas Control*, **12**, 155-167.
- Ringrose, P., M. Atbi, D. Mason, M. Espinassous, O. Myhrer, M. Iding, A. Mathieson, and I. Wright (2009), Plume development around well KB-502 at the In Salah CO₂ storage site, *First Break*, **27**, 85–89.
- Rosen, P.A., S. Hensley, I.R. Joughin, F.K. Li, S.O. Madsen, E. Rodriguez, and R.M. Goldstein (2000), Synthetic aperture radar interferometry, *Proc. IEEE*, **88**, 333-382.
- Rucci, A., D.W. Vasco, and F. Novali (2013), Monitoring the geologic storage of carbon dioxide using multicomponent SAR interferometry, *Geophys. J. Int.*, **193**, 197-208.
- Rutqvist, J., HJ-H Liu, D.W. Vasco, L. Pan, K. Kappler, and E. Majer (2011), Coupled non-isothermal, multiphase fluid flow, and geomechanical modeling of surface deformations and potential for induced seismicity at the In Salah CO₂ storage operation, *Energy Procedia*, **4**, 3542-3549.
- Shi, J-Q., C. Sinayuc, S. Durucan, and A. Korre (2012), Assessment of carbon dioxide plume behavior within the storage reservoir and the lower caprock around the KB-502 injection well at In Salah (2012), *Int. J. Greenhouse Gas Control*, **7**, 115-126.
- Vasco, D. W., A. Ferretti, and F. Novali (2008), Estimating permeability from quasi-static deformation: Temporal variations and arrival-time inversion, *Geophysics*, **73**, O37– O52.

Vasco, D. W., A. Rucci, A. Ferretti, F. Novali, R. C. Bissell, P. S. Ringrose, A. S. Mathieson, and I. W. Wright (2010), Satellite-based measurements of surface deformation reveal fluid flow associated with the geological storage of carbon dioxide, *Geophys. Res. Lett.*, **37**, L03303, doi:10.1029/2009GL041544.

Wright, I. (2006), Two years of geologic storage at In Salah, in *Proc. 8th Int. Conf. on Greenhouse Gas Control Technology, Trondheim, Norway, 19-22 June*.

Wright, T.J., B.E. Parsons, and Z. Lu (2004), Toward mapping surface deformation in three dimensions using InSAR, *Geophys. Res. Lett.*, **31**, 1-5.

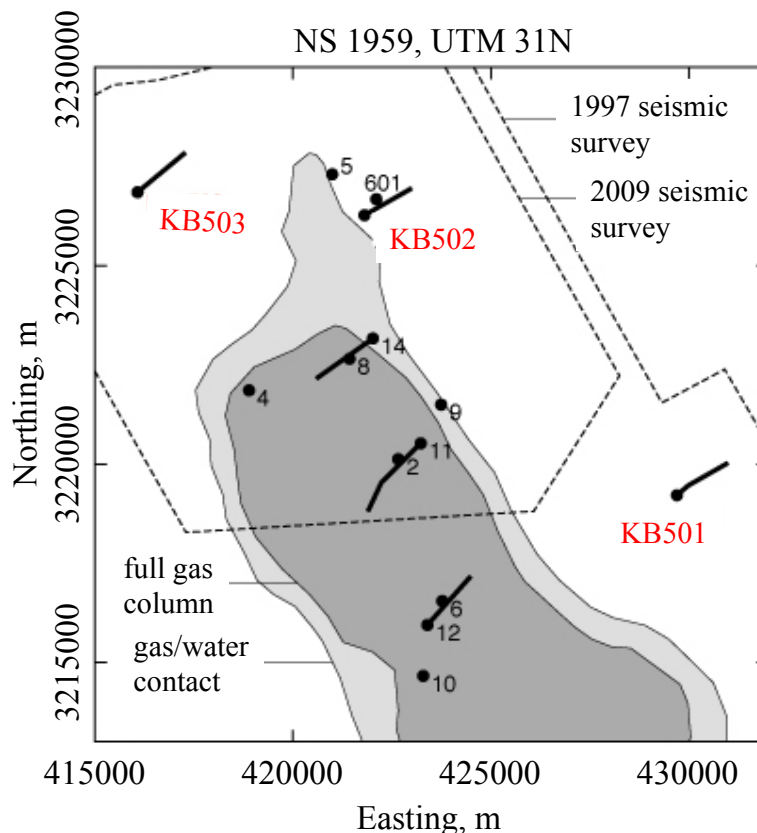


Figure 1: Layout of the Krechba field. Injector wells labeled in red.

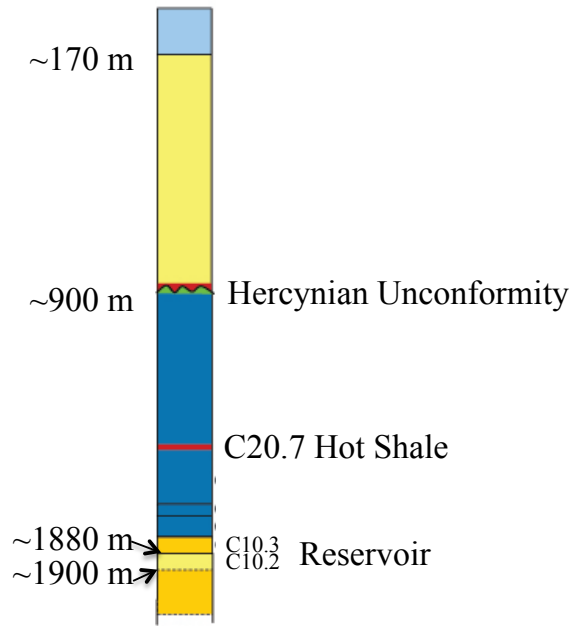


Figure 2: Krechba stratigraphy (courtesy In Salah JIP).

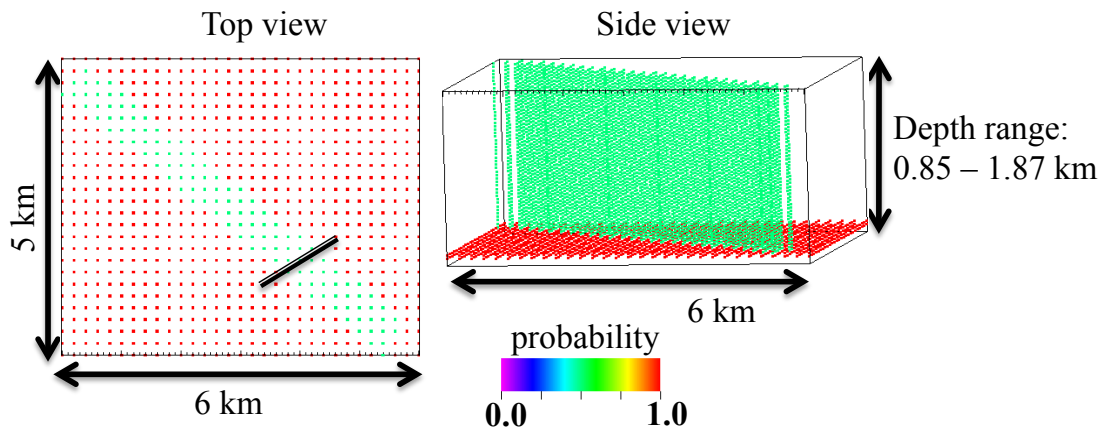
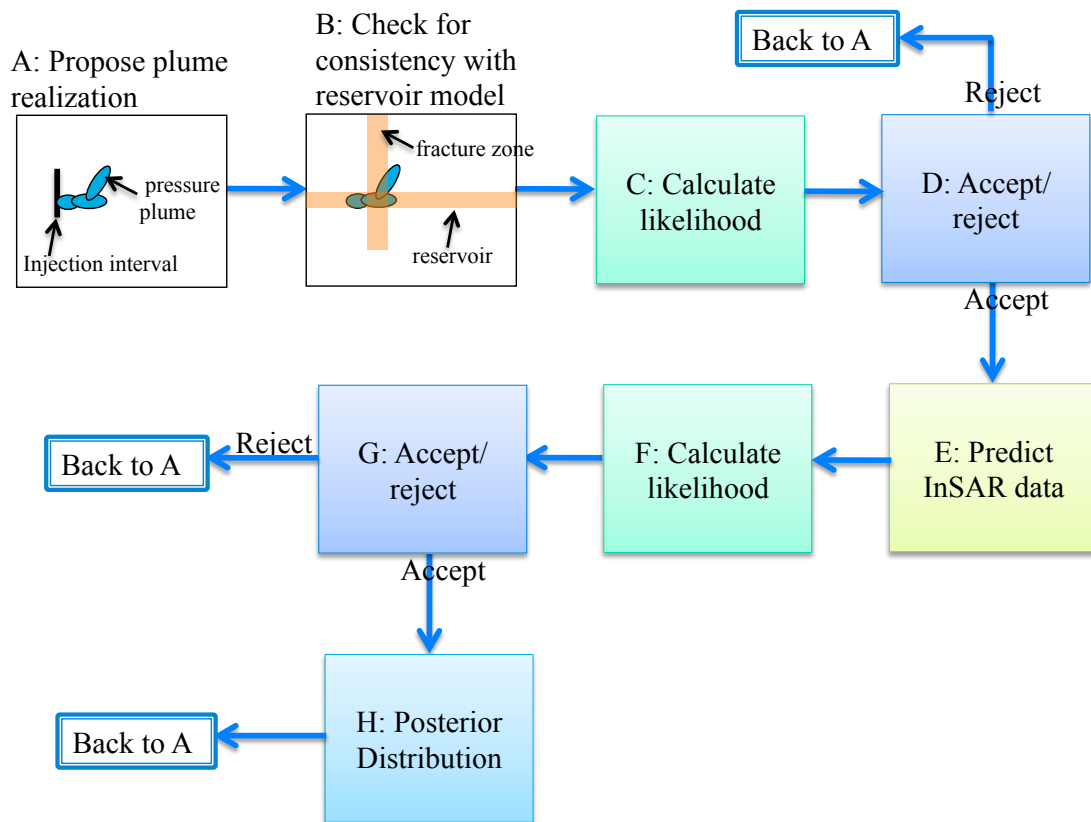


Figure 3: Structural model used in synthetic modeling and stochastic inversions. The model assumes that it is certain that overpressures will exist in the reservoir (red nodes) and probable that the plume will penetrate the vertical zone within the reservoir and lower caprock (green nodes). The horizontal black line shows the approximate location of the KB-502 injection interval.

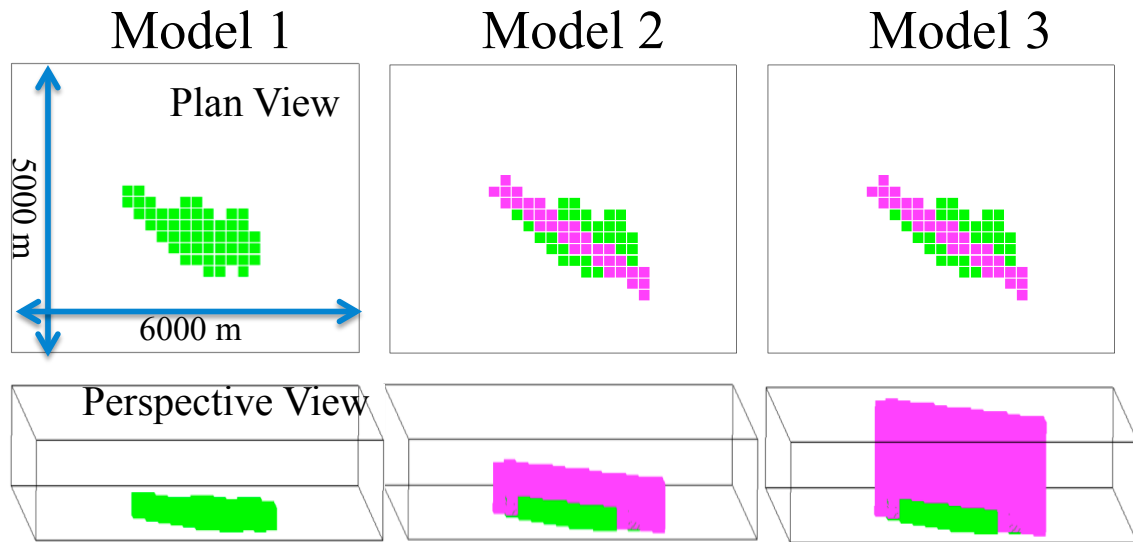
1000
1001
1002
1003
1004
1005
1006
1007
1008
1009
1010
1011



1012
1013
1014
1015
1016
1017
1018
1019
1020
1021
1022
1023
1024

Figure 4: Schematic of the MCMC procedure as adapted for inversion of In Salah InSAR data. The process starts (upper left) by proposing pressure plume realizations that honor simple rules. Realizations that are consistent with the reservoir model (step B) are used to predict InSAR data (step E). Realizations that produce InSAR data that are acceptably close to the observations become part of the posterior distribution.

1025
1026
1027
1028



1029
1030
1031
1032
1033
1034
1035
1036
1037
1038
1039

Figure 5: Plan (*top*) and perspective (*bottom*) views of the 3 three overpressure models used in the synthetic modeling. The height of the box is 1020 m. The *green* and *pink* elements indicate the pressurized regions in the reservoir layer and vertical zone, respectively: Model 1 (*left*), overpressure zone is fully contained within the reservoir; Model 2 (*center*), overpressure extends 300 m above the reservoir into the lower cap rock; Model 3 (*right*), overpressure extends 940 m from the reservoir to reach the HU.

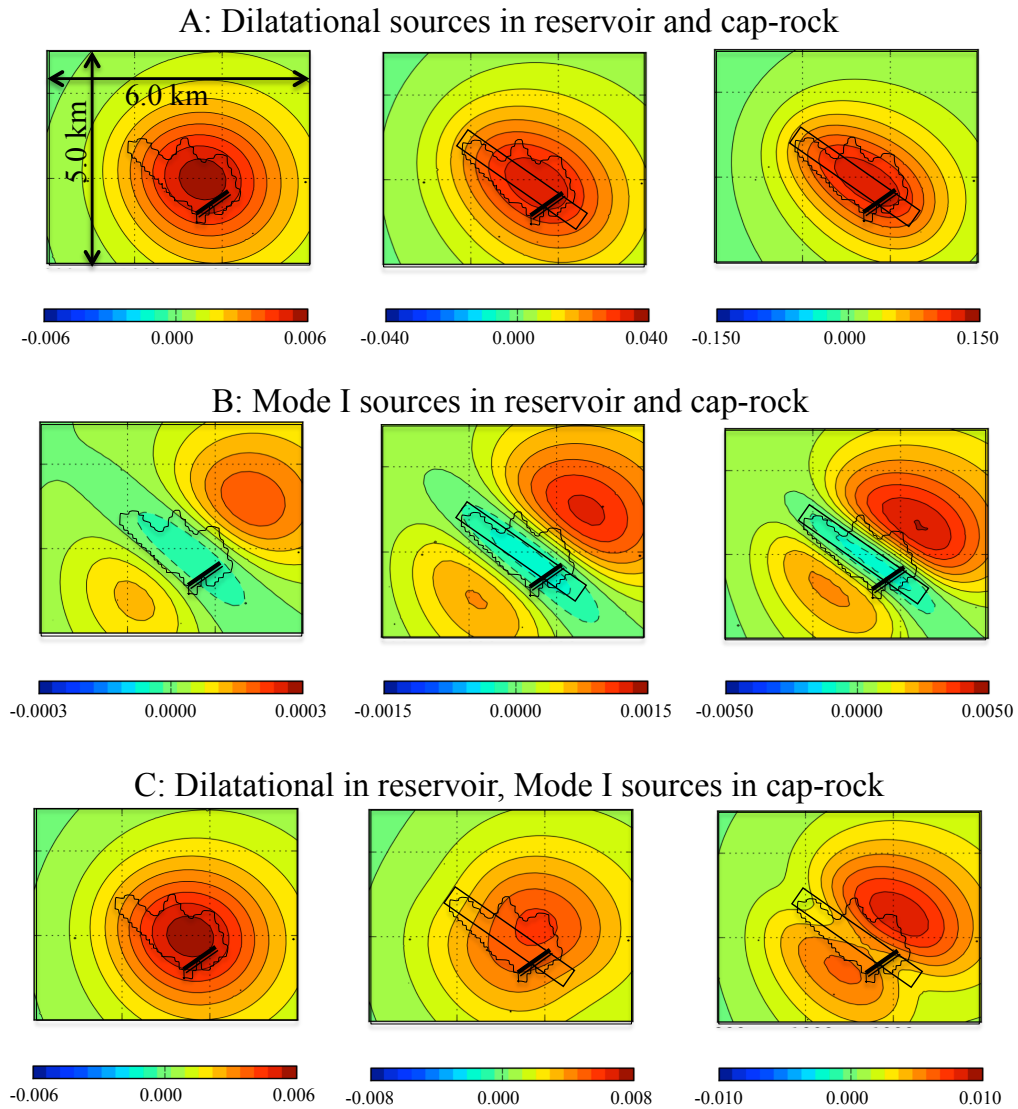
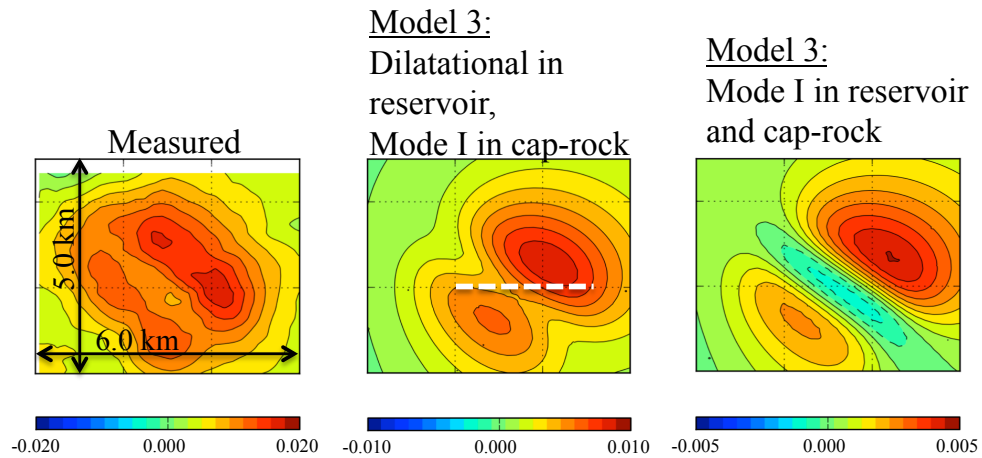


Figure 6: Calculated InSAR range change for Models 1 - 3 (*left to right*) for 3 deformation scenarios: (*A*) all deformation sources in reservoir and cap-rock are dilatational; (*B*) all deformation sources in reservoir and cap-rock are Mode I; and (*C*) deformation sources in the reservoir are dilatational and Mode I in the cap-rock. Positive range change indicates that the distance between the satellite and the surface is shorter; i.e. uplift. Note that the color scale (range change in m) is different for each of the images. The irregular thin black lines superimposed on the images show the outlines of the overpressure plumes. The thick black line shows the location of a hypothetical injection well.

1056
1057
1058
1059
1060
1061
1062
1063
1064



1065
1066
1067
1068
1069
1070
1071
1072
1073
1074
1075
1076
1077
1078

Figure 7: Comparison between observed range changes derived from Envisat data above KB-502 between March and July 2007 (*left*) with synthetics calculate from dilatational and Mode I sources in the reservoir and fracture zone, respectively (*middle*), and Mode I source in both the reservoir and fracture zone (*right*). The dashed line on the *middle* panel shows the transect line used for Figure 8.

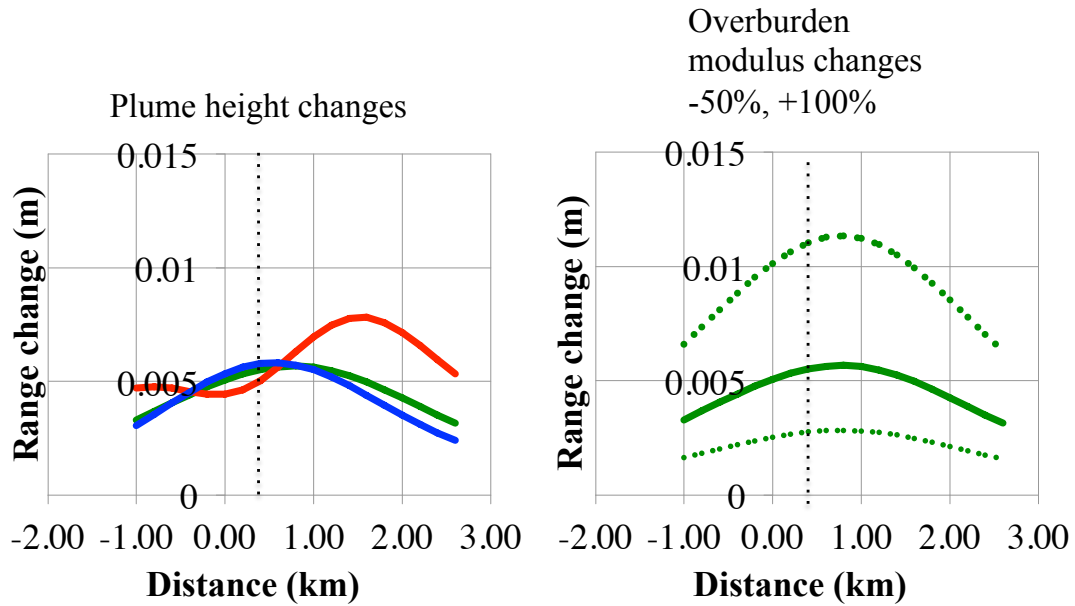


Figure 8: Sensitivity of InSAR range change to uncertainties in overburden properties. (*left*) variation in line-of-sight range change along the transect line shown in Figure 7 for the three dual-source models. (*right*). Variation in range change along the same transect for Model 2 (pressure penetrates 300 m above the reservoir) calculated for the base half-space elastic model (*solid curve*), and double (*dotted*) and half *dashed*) the base shear modulus value. The black dotted line indicates the position of the vertical fracture zone.

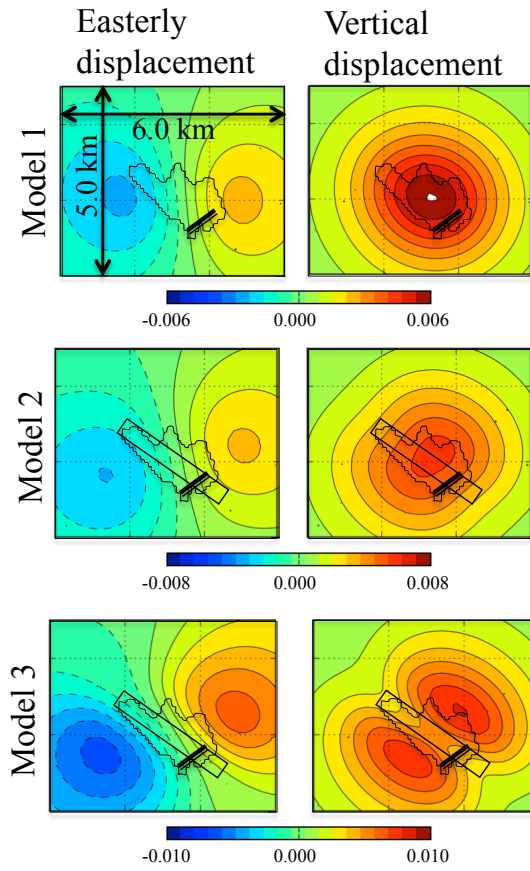


Figure 9: Quasi-easterly (*left*) and quasi-vertical displacements (*right*) calculated for models 1 - 3 (top to bottom) and the dual-mode scenario. Positive vertical displacements indicate uplift and positive Easterly displacements indicate movement to the East. Each color scale shows displacement in meters and is different for each row of images.

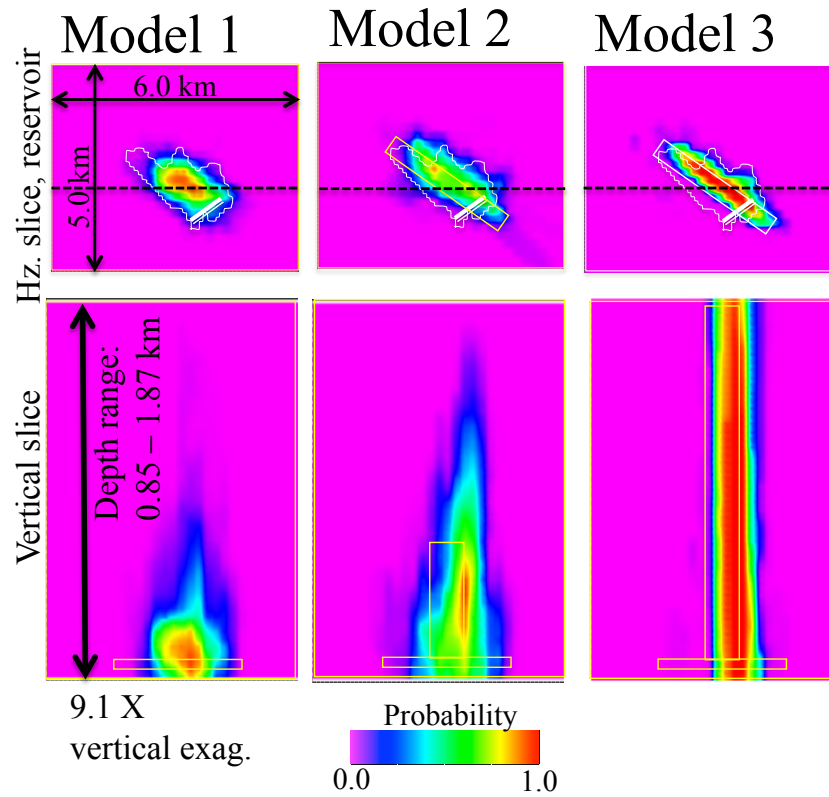
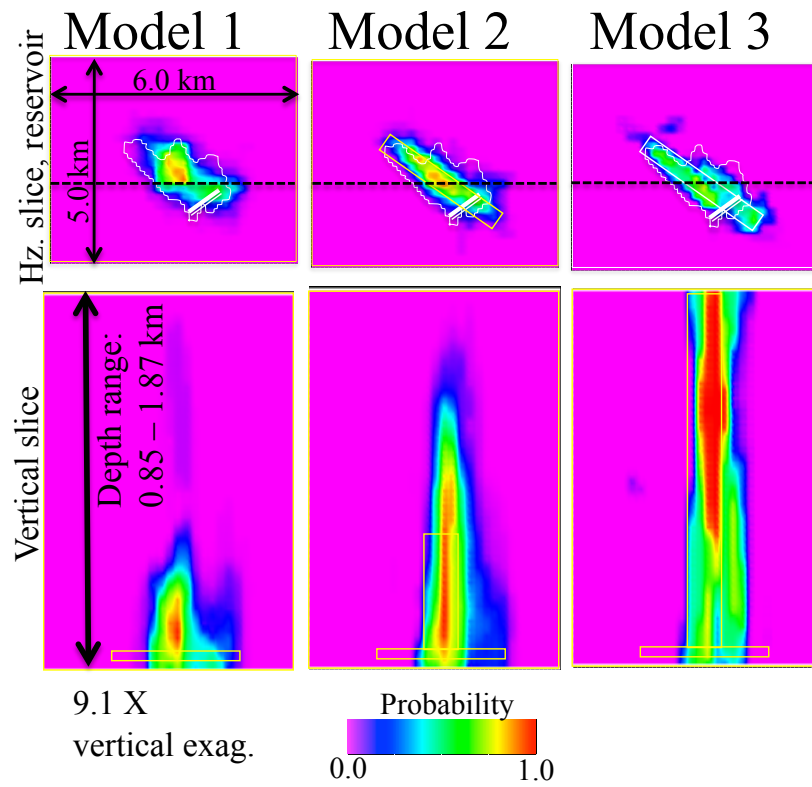


Figure 10: Results of inverting synthetic InSAR range-change data generated by the three synthetic reservoir models shown in Figure 5 and a dual-source scenario. The plots show the probability that the pressure plume exists at each node in the inversion grid (see text). (*top*) horizontal slices located at reservoir depth. White outlines superimposed on each plot outline the true shape of the pressure perturbation at the depth of the slice. The dashed line shows the location of vertical slices (*bottom*) (vertical exaggeration 9x).

1131
1132
1133



1134
1135
1136
1137
1138

Figure 11: Results of inverting synthetic two-component displacements generated as for Figure 10. See Figure 10 caption for explanation.

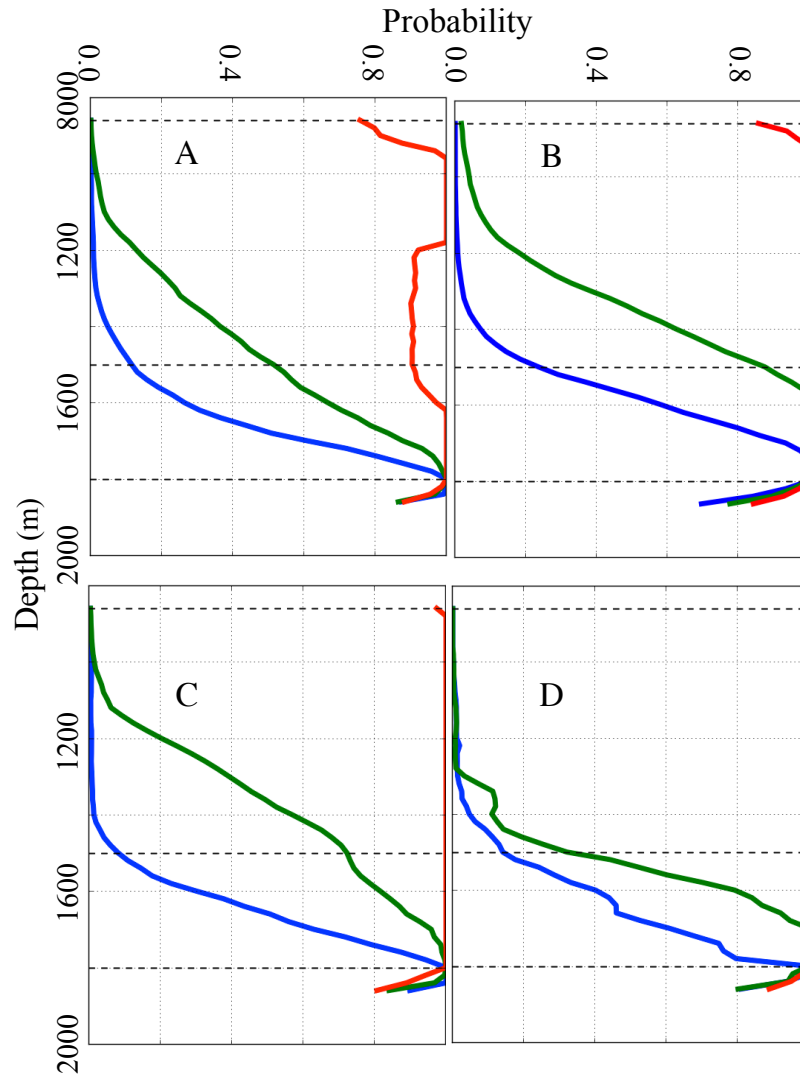
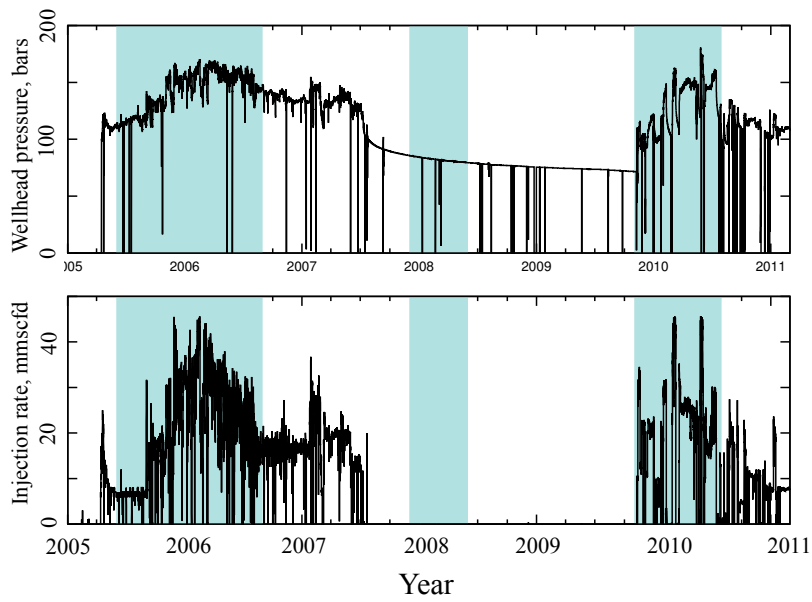


Figure 12: Estimates of probability that a pressure perturbation exists in the synthetic inverse solutions from: (A) LOS data and a dual-source scenario; (B) LOS and dilatational source only; (C) quasi-EW and quasi-vertical displacements and a dual-source scenario; (D) as in C with shear modulus uncertainty of -50% to +100% (the shear modulus variation for (A, B, C) is $\pm 11\%$). Blue, green, and red curves correspond to Models 1, 2 and 3, respectively. Dashed horizontal lines indicate, from deep to shallow, the tops of Models 1 (top reservoir), 2 (300 m above reservoir) and 3 (940 m above reservoir).

1156
1157
1158
1159



1160
1161
1162
1163
1164
1165
1166
1167
1168
1169
1170
1171
1172
1173

Figure 13: KB-502 wellhead pressure (top) and injection rate (bottom) as a function of time. The light blue boxes define the time intervals of the In SAR images used for the inversions.

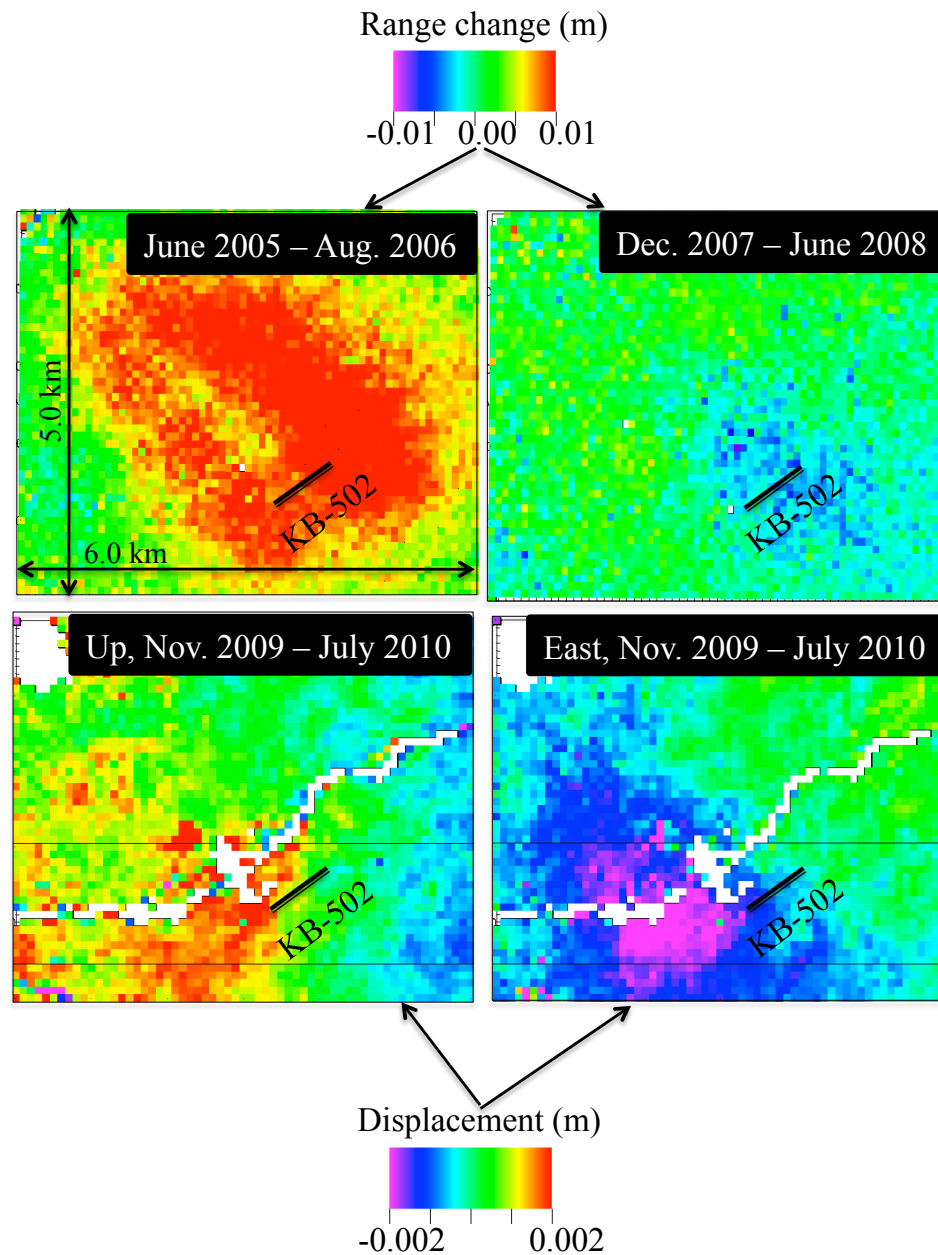
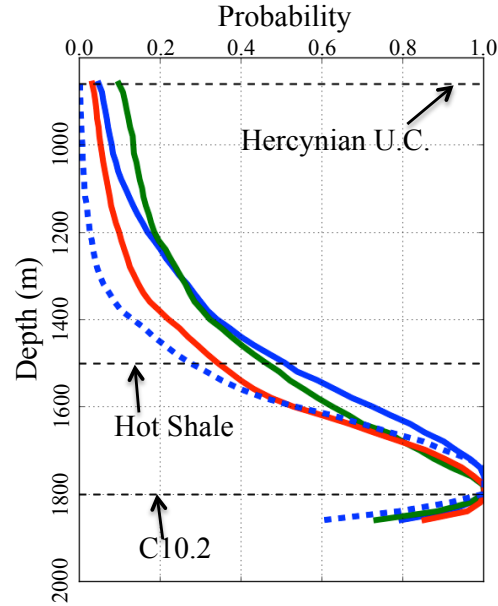


Figure 14: InSAR images used for inversions over three time periods. (*top*) Envisat Track 294 PSInSAR range changes between June 2005 and August 2006 (*left*) and December 2007 and June 2008 (*right*). (*bottom*). Quasi-vertical (*left*) and quasi-east-west (*right*) displacements derived from SqueeSAR® processing of Cosmos-SkyMed data. The white colored pixels have been removed because they show displacements that are likely associated with surface processes such as seasonal moisture changes in wadis.



- Cap-rock mode 1 sources, 6 ell., floating strike, dip
- Cap-rock mode 1 sources, 6 ell., fixed strike, dip
- Cap-rock mode 1 sources, 3 ell., fixed strike, dip
- - - Cap-rock dilatational sources, 6 ell.

Figure 15: Probability that the pressure plume extends to different caprock depths derived from inversion of range-change data for the period 6/2005 – 8/2006. *Solid* curves correspond to inversions using the dual-source scenario. The inversion corresponding to the *solid blue* curve allowed the strikes and dips of opening-mode sources to vary, while in the inversions resulting in the *green* and *red* curves they were held fixed at the strike and dip reported by Iding and Ringrose (2012). *Dashed* curve corresponds to an inversion using only dilatational sources. The depths of the reservoir (C10.2), Hot Shale, and HU are shown for reference.

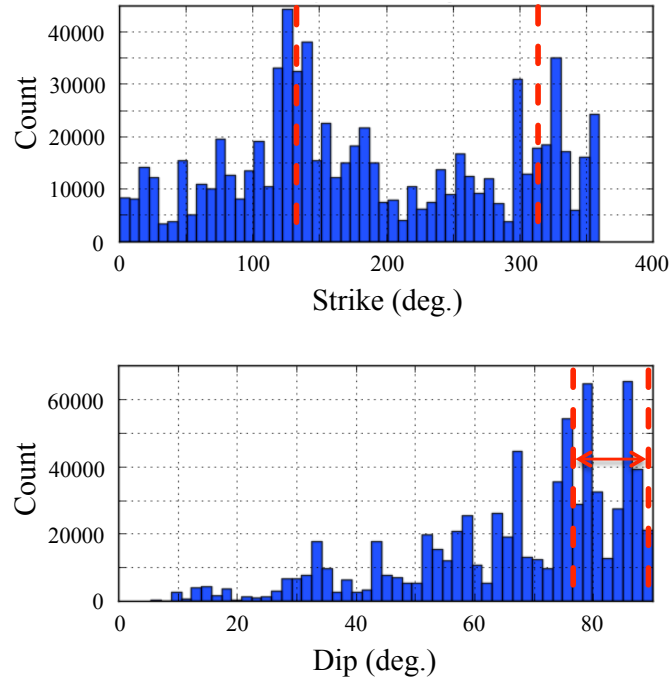


Figure 16: Histograms of strike (*top*) and dip (*bottom*) recovered by a stochastic inversion in which the strikes and dips of opening-mode sources were sampled from uniform distributions over the ranges $\pm 180^\circ$ and $\pm 90^\circ$, respectively. The red dashed lines indicate the predominant fracture strike and dip angles reported by Iding and Ringrose (2010).

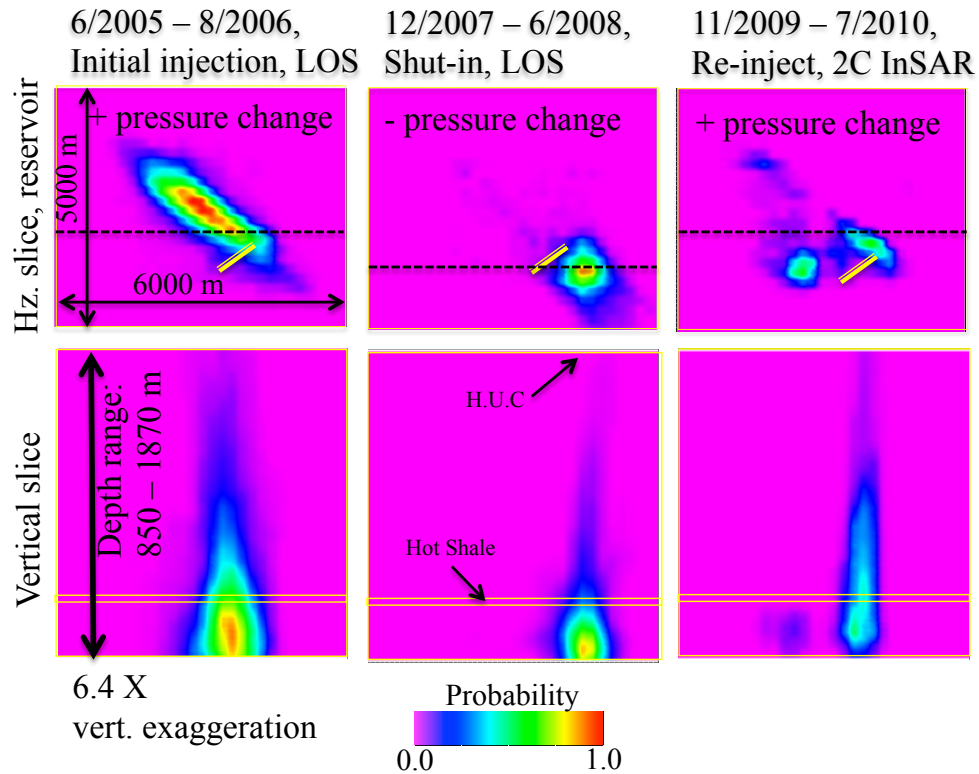


Figure 17: Inversion results using In Salah field data during the initial injection (*left*), during shut-in (*center*), and during the early part of the second injection phase (*right*). The plots show the probability that a pressure perturbation exists at each node in horizontal slices through the inversion grid at reservoir depth (*top*) and in vertical slices (*bottom*); dashed lines show the locations of the vertical slices. A short yellow line identifies the KB-502 injection interval. Vertical slices show approximate locations of the Hot Shale and Hercynian Unconformity; the reservoir layer is located just above the bottom edge of each slice.

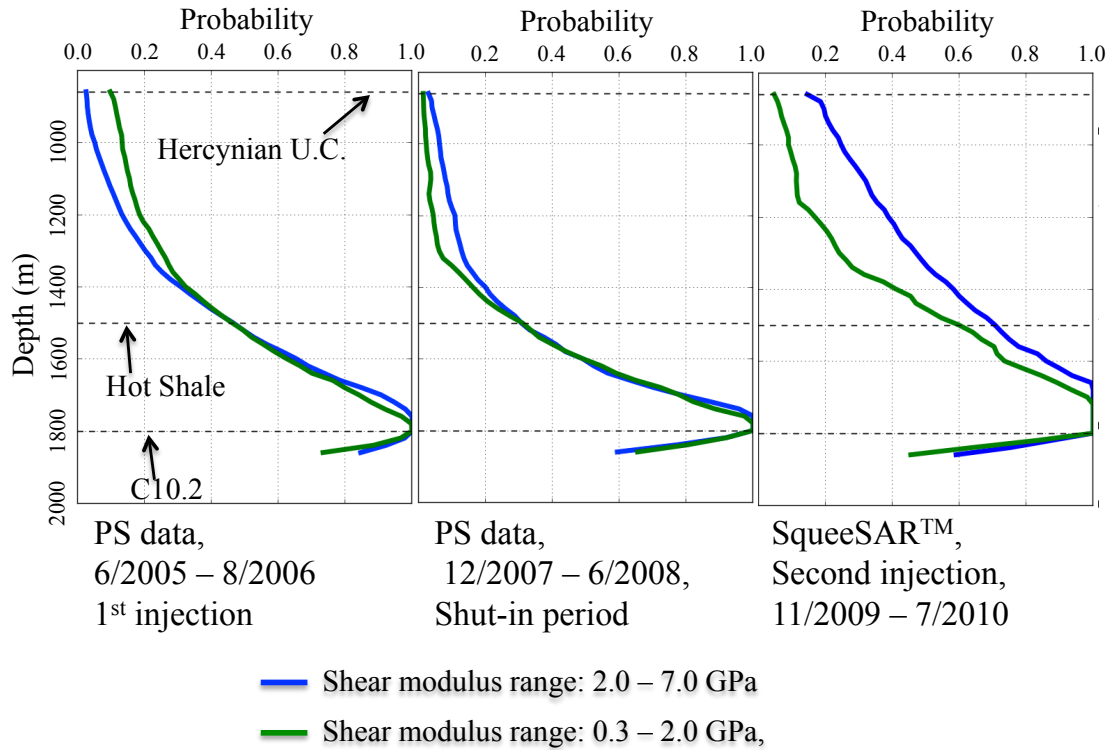


Figure 18: Estimated probability that the pressure plume extends to different cap-rock depths for the three time periods defined in Figure 11. The *green* and *blue* curves show estimates assuming two different shear modulus ranges, 0.3 – 2.0 GPa and 2.0 – 7.0 GPa, respectively.

1235
1236
1237
1238